

Available online at www.sciencedirect.com

jmr&t
Journal of Materials Research and Technology

journal homepage: www.elsevier.com/locate/jmrt**Original Article****Structure and properties of the CrMnFeCoNi high-entropy alloy irradiated with a pulsed electron beam**

V.E. Gromov ^{a,*}, S.V. Konovalov ^b, Yu.F. Ivanov ^c, Yu.A. Shliarova ^a,
S.V. Vorobyov ^a, A.P. Semin ^a

^a Siberian State Industrial University, 654007 Novokuznetsk, Russia

^b Samara National Research University, 443086 Samara, Russia

^c Institute of High-Current Electronics, SB RAS, 634055 Tomsk, Russia

ARTICLE INFO**Article history:**

Received 20 March 2022

Accepted 20 June 2022

Available online 26 June 2022

ABSTRACT

According to the technology of wire-arc additive manufacturing a nonequiautomic composition CoCrFeMnNi high-entropy alloy (HEA) was obtained. Deformation curves of samples in tension are plotted and analyzed after the HEA fabrication by the methods of wire-arc additive manufacturing (initial state) and after the electron-beam processing (EBP). The EBP results in a decrease in the HEA's strength and plastic properties. Along with a pit character of the fracture a presence of micropores and microlayerings are identified. A study of the HEA's fracture surface after the EBP except for regions with a ductile fracture mechanism revealed regions with a band (lamellar) structure. The area with a band structure increases with a growth in the beam electron density from 25% at 10 J/cm² to 65% at 30 J/cm². A diameter of separation pits in fracture bands varies in the limits (0.1–0.2) μm, which is considerably less than those of the remaining part of the HEA sample. An average size of crystallization cells formed in the EBP depends on the energy density of electron beam and increases from 310 nm at 15 J/cm² to 800 nm at 30 J/cm². A non-monotonous change in the scalar dislocation density, reaching a maximum value of ~5.5 · 10¹⁰ cm⁻² at a distance of 25 μm from the irradiation surface is revealed. It is suggested that defects being formed in surface layers in the EBP may be one of the reasons for decreasing the values of HEA strength and plasticity.

© 2022 The Authors. Published by Elsevier B.V. This is an open access article under the CC BY-NC-ND license (<http://creativecommons.org/licenses/by-nc-nd/4.0/>).

1. Introduction

In recent years the attention of scientists is attracted by a new system of alloys known as high-entropy alloys (HEA) [1–8]. In contrast to conventional alloys the high-entropy alloys

consist of five and more main elements with a percentage from 5 to 35 at.% [9–14]. The idea of high-entropy alloys lies in the fact that atoms of all elements are supposed to be atoms of a dissolved substance, they cause deformation of a crystal structure and improve a thermodynamic stability of properties related to differences in atomic radii of components. It

* Corresponding author.

E-mail address: gromov@physics.sibsiu.ru (V.E. Gromov).

<https://doi.org/10.1016/j.jmrt.2022.06.108>

2238-7854/© 2022 The Authors. Published by Elsevier B.V. This is an open access article under the CC BY-NC-ND license (<http://creativecommons.org/licenses/by-nc-nd/4.0/>).

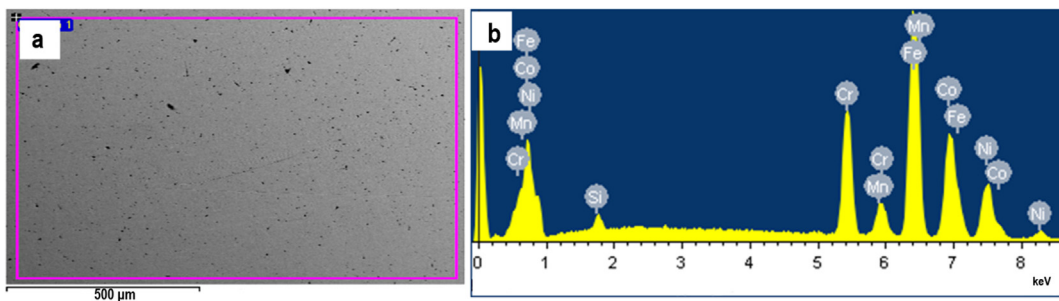


Fig. 1 – An electron microscopic image of the HEA part (a) and energy spectra obtained from the part (b).

leads to a high entropy of the system for a further manufacturing of the material with unique properties that are impossible in traditional methods of microalloying [15–18].

The original results obtained in the HEA field have been considered in detail in analytical reviews and monographs [1,19–23] where the HEA structure, properties and thermodynamics are described, results of modeling of their structure are analysed and new variants of methods for manufacturing multicomponent alloys are discussed. The HEA studies have shown that a formation of nano-dimensional structures and even amorphous phases is possible in them due to significant lattice distortions caused by a difference in atomic radii of substitutional atoms [1,22].

One of the first high-entropy alloys under study is the CoCrFeMnNi alloy which is capable of retaining a face-centered cubic structure in a wide temperature range and possesses a good balance of strength and plasticity as well [24]. In the paper [25] it has been demonstrated that the alloy shows simultaneously an increase in strength at a room temperature and ductility at cryogenic (77 K) temperature as a result of dominating of twinning as a mechanism of deformation. However, a disadvantage of the CoCrFeMnNi-system alloys is a relatively low yield point at room temperature. In different works the strengthening alloying elements such as Ti, Si, Cu, C [26–28] were used as methods for increasing the yield point. Various methods of surface processing among which the ultrasonic effect [29], nitriding [30], ion implantation [31] and boriding [32] shown an effective application for increasing the fatigue life, strength and corrosion resistance of metallic alloys. Nevertheless, the methods require an accurate control of chemical composition and manufacturing technology, which is often costly and infeasible for industrial application. The electron-beam processing is one of the perspective methods of a surface modification of metallic materials leading to a substantial increase in metallic properties of an entire material at the expense of a structural

optimization of its surface layer [33]. Characteristics of metals and alloys subjected to irradiation with an electron beam may increase by a factor of 20, which increases substantially the efficiency of traditional types of processing [34]. In an irradiation process the electron beams of a high density cause different phenomena in a surface layer such as the high-velocity recrystallization, surface smoothing, and annealing [35] during an extremely short period of time. In addition, the electron-beam processing may induce a plastic deformation of a near-surface layer, which results in a formation of dislocations with a high density and a significant improvement of properties [36,37].

The electron-beam processing ensures ultrahigh speeds of heating (to 10^6 K/s) of a surface layer to preset temperatures and cooling a surface layer at the expense of a heat removal to a material bulk at rates of 10^4 – 10^9 K/s, with the result that nonequilibrium submicro- and nano-crystalline structural phase states form in a surface layer.

At a given point of time a limited number of scientific papers are devoted to a study of the effect of the electron-beam processing on high-entropy alloys. For instance, it is shown in the paper [38] that the wear resistance, microhardness, nanohardness, and corrosive properties of the CoCrFeNiMo_{0.2} alloy underwent an appreciable increase as a result of an electron-beam effect. The irradiation of the NiCoCrAlYSi alloy with a high-current electron beam in the paper [39] resulted in a formation of a dense remelted surface layer and a removal of initial defects originating in a laser surfacing. It was earlier shown by the team of authors of the paper that the electron-beam processing results in homogenization of a chemical composition of the CoCrFeMnNi-system high-entropy alloy [40].

The aim of the research is to study structural phase state of the defective substructure, fracture surface and properties of the CrMnFeCoNi high-entropy alloy subjected to the electron-beam processing.

Table 1 – An elemental composition of the HEA sample part obtained by the methods of micro-X-ray spectral analysis.

| Element | Weight, % | | Atomic, % | |
|---------|--------------------|------|---|------|
| | Before irradiation | | After irradiation $E_s = 30 \text{ J/cm}^2$ | |
| Cr K | 14.3 | 15.5 | 14.3 | 15.5 |
| Mn K | 3.0 | 3.1 | 3.0 | 3.1 |
| Fe K | 38.4 | 38.9 | 37.8 | 37.9 |
| Co K | 25.7 | 24.6 | 27.0 | 26.0 |
| Ni K | 18.6 | 17.9 | 17.9 | 17.5 |

2. Material and methods of investigation

A high-entropy alloy (HEA) of the CrMnFeCoNi-elemental composition was used as a test material. The alloy was fabricated by the method of wire-arc additive manufacturing (WAAM) [22]. A three-strand wire was used as an initial material to fabricate the Co–Cr–Fe–Mn–Ni system samples. It consisted of a pure cobalt wire (\approx 99.9 at.% Co) 0.47 mm in diameter; a welding wire Autrod 16.95 (\approx 65.3 at.% Fe, \approx 19.6 at.% Co, \approx 7.3 at.% Ni, \approx 1.6 at.% Si, \approx 6.2 at.% Mn) that was preliminary thinned from 0.80 up to 0.74 mm in diameter; a chromium-nickel wire Ni₈₀Cr₂₀ (\approx 22.5 at.% Cr, \approx 1.5 at.% Fe, \approx 72.1 at.% Ni, \approx 0.8 at.% Al, \approx 2.9 at.% Si, \approx 0.2 at.% Mn) of 0.4 mm in diameter. Initial wires were twisted by means of a special twisting device. A diameter of the Co–Cr–Fe–Mn–Ni composite cable amounted to \approx 1.25 mm, with a length of laying 10 mm. A fabrication of HEA samples was performed by layer-by-layer application on the 12Kh18N10T (18% wt. Cr, 10% wt. Ni, 1% wt. Ti, 0.12% wt. C) steel substrate by a technology of the wire-arc additive manufacturing in atmosphere of inert gas (Ar \approx 99.99%). The following regime of layers' application was used: the feed rate of wire 13 m/min, voltage 22 V, rate of motion of a burner 0.1 m/min. The obtained high-entropy alloy had sizes of 140 \times 20 \times 30 mm and presented a parallelepiped consisting of seven surfaced layers in height and four layers in thickness. Tensile tests were performed on flat proportional

samples in the form of a two-sided blade according to Russian State Standard 1497–84 [41]. Samples were cut from a massive blank by the methods of electroerosion cutting. Before tests the samples had the following sizes: 1.05 mm in thickness; 4.4 mm in width; a length of a working part 8.0 mm. A part of samples was irradiated from two sides (working part) on a plant 'SOLO' developed and fabricated at Institute of High-Current Electronics SB RAS [42]. The irradiation regimes were the following: the energy density of electron beam (10, 15, 20, 25, 30) J/cm², duration of a pulsed beam 50 μ s, pulse number 3, pulse repetition rate 0.3 s⁻¹. The irradiation was carried out in an argon medium at a residual pressure of 0.02 Pa. A deformation of samples was done by uniaxial tension on a test installation Instron 3369 (rate of tests 1.2 mm/min; temperature 22 °C) with an automatic recording of a stress–strain curve.

1A structural phase state of the initial and irradiated samples as well as those failed as a result of a tensile test were studied by the methods of scanning electron microscopy (device 'LEO EVO 50' (Carl Zeiss) equipped by energy-dispersive analyzer INCA-energy), transmission electron microscopy (device JEOL JEM-2100, Japan), X-ray structural analysis (diffractometer XRD-6000). Subjected of research foils 150–200 nm thick for a transmission electron microscope were fabricated by the method of ion etching (plant Ion Slicer (EM-09100IS), argon) of plates cut from the HEA sample under study. The X-ray photography was done

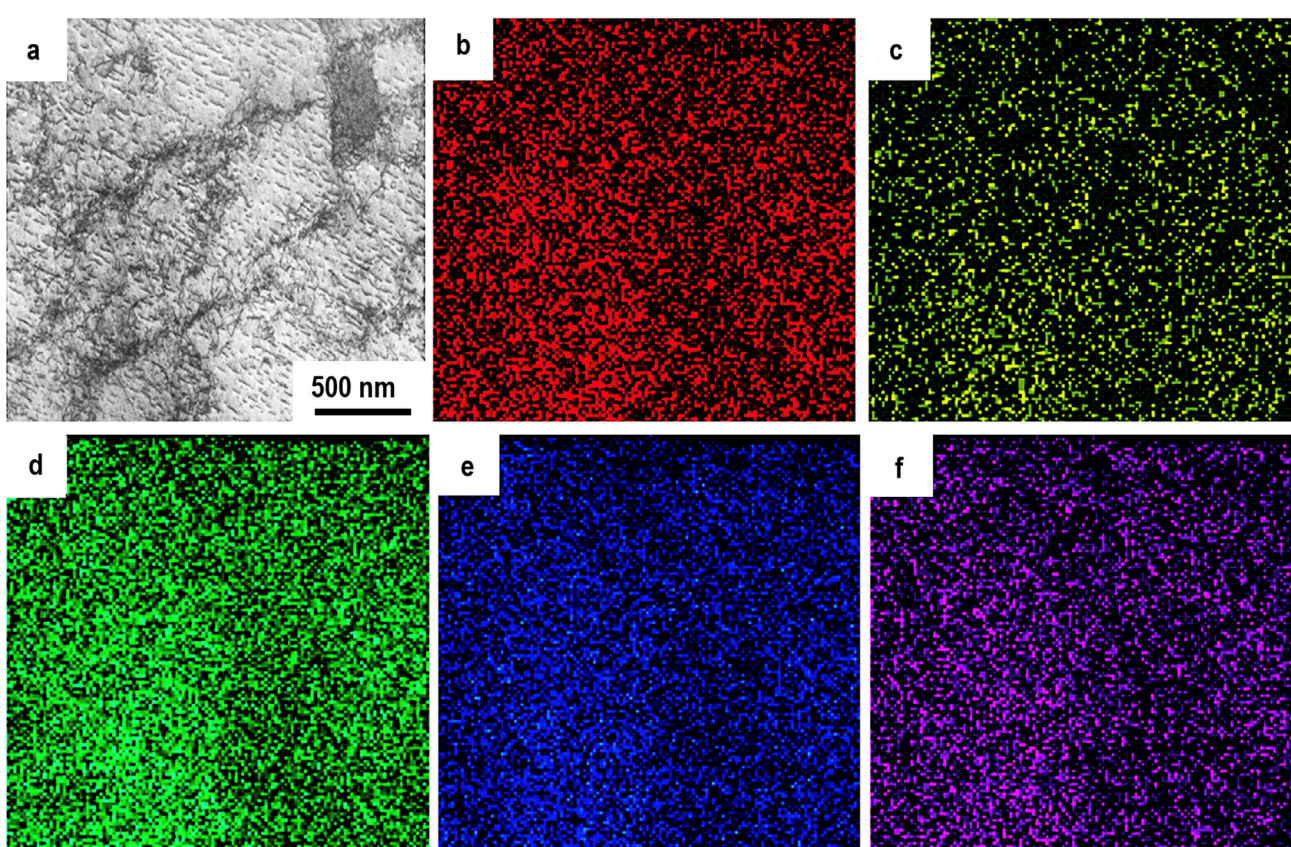


Fig. 2 – STEM analysis image of a foil portion (a); b-f – foil portions obtained in a characteristic radiation of Cr (b), Mn (c), Fe (d), Co (e), Ni (f) atoms.

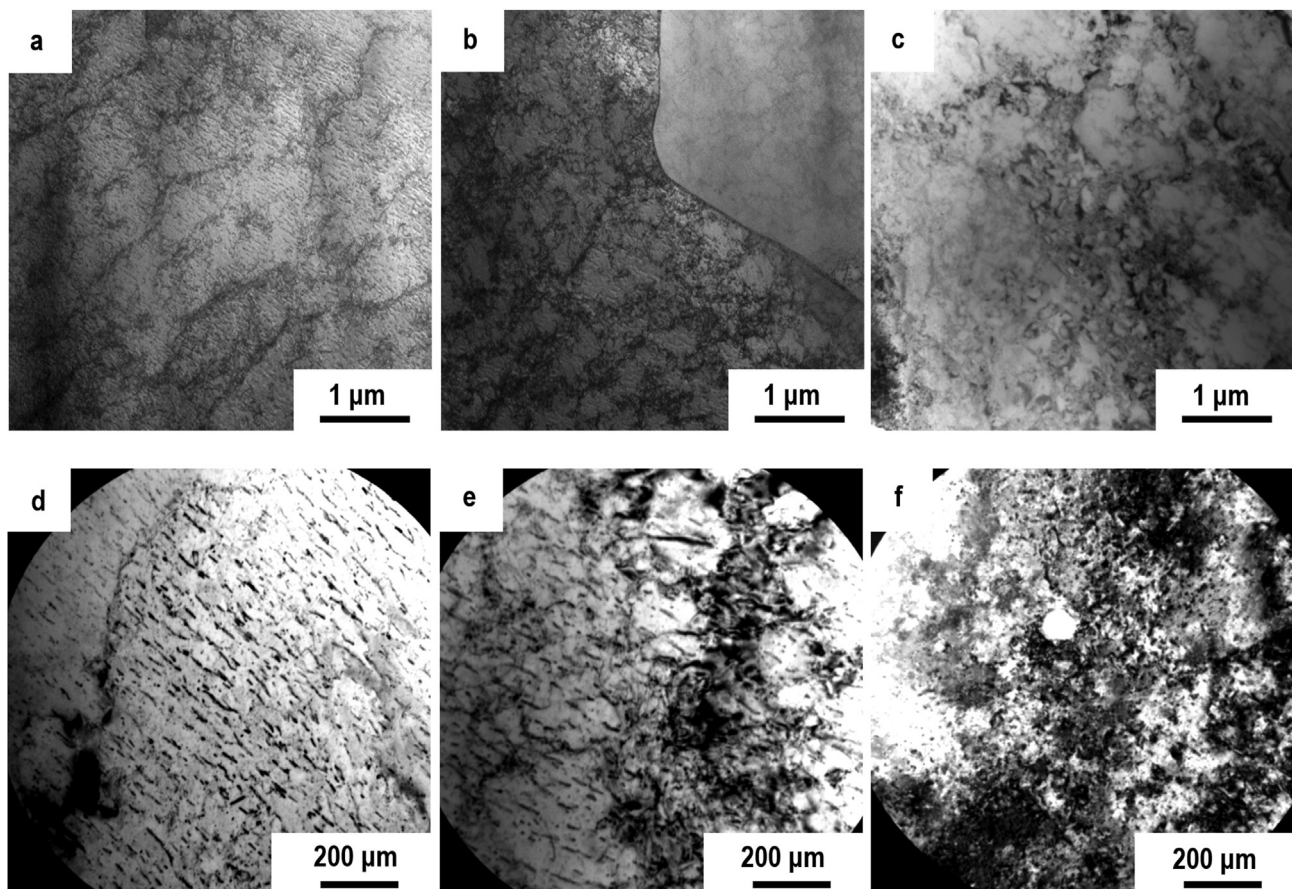


Fig. 3 – A dislocation substructure of the Co–Cr–Fe–Mn–Ni-system high-entropy alloy irradiated with a pulsed electron beam; a, d – a surface; b, e – at a distance of 25 μm ; c, f – at a distance of 45 μm .

on CuK α irradiation according to the Bragg–Brentano scheme with the pitch 0.03°, time of exposition at a point 0.5 s and angular range 25° ÷ 90°. A voltage on a X-ray tube amounted to 40 kV, a beam current 30 mA. Calculations of intensities were performed by the Rietveld method. A phase

composition determination was carried out using data base PDF 4+ as well as a program of full-profile analysis POWDER CELL 2.4. A surface microhardness of irradiated samples was detected by the Vickers method on a device PMT-3.

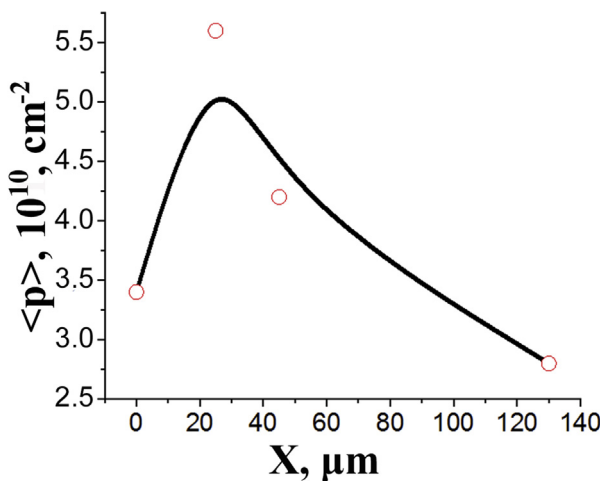


Fig. 4 – A scalar dislocation density as a function of a distance from an irradiation surface of the Co–Cr–Fe–Mn–Ni – system high-entropy alloy.

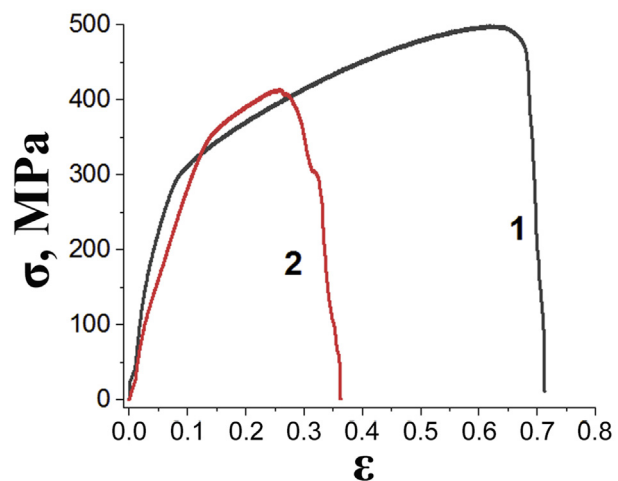


Fig. 5 – Deformation curves obtained in tension of the HEA in the initial state (curve 1) and after irradiation with a pulsed electron beam (curve 2), $E_s = 30 \text{ J/cm}^2$.

3. Results and discussion

The HEA elemental composition was determined by the methods of micro-X-ray spectral analysis (Fig. 1).

Quantitative results of the X-ray microspectral analysis are listed in Table 1. When analyzing the results presented in Table 1 it is noted that, firstly, the obtained alloy belongs to nonequiautomic-composition alloys in relation to chemical elements. Secondly, an irradiation of the alloy with a pulsed electron beam results in a redistribution of chemical elements in a surface layer, namely, in a decrease in a concentration of iron and nickel atoms, and an increase in a concentration of cobalt atoms.

A homogeneous distribution of the listed elements in a bulk of the alloy (Fig. 2) is detected by the mapping methods.

Studies of a defective substructure being formed in the HEA's sample irradiation with a pulsed electron beam were carried out by the methods of transmission electron microscopy. It is shown that a nondisoriented cellular dislocation substructure (Fig. 3, a, d) forms in a surface layer. A cell size varies in the limits from 400 nm to 600 nm. Chaotically distributed dislocations are detected in a bulk of cell. A similar cellular dislocation substructure was observed in the NiCoCrAlYSi alloy after the electron beam processing [22]. A nondisoriented cellular-netlike dislocation substructure (Fig. 3, b, e) forms at a depth of 25 μm. With a further increase in a distance from an irradiation surface by 45 μm, a substructure formed by dislocations distributed chaotically (Fig. 3, c, f) is present along with a cellular-netlike dislocation substructure. At a distance of 120–130 μm from an irradiation surface the dislocation structure corresponds to an initial state and presents chaotically distributed dislocations (Fig. 3, a) with a dislocation density of $\sim 2.7 \cdot 10^{10} \text{ cm}^{-2}$ (Fig. 4). When analyzing the results presented in Fig. 3 it is noted that a scalar dislocation density decreases with a greater distance from an irradiation surface.

A scalar dislocation density as a function of an irradiation surface is depicted in Fig. 4. Analysing the presented results a nonmonotonous change in a scalar dislocation density is noted with a greater distance from the irradiation surface. One of the reasons for the dependence may be a substantially inhomogeneous distribution of dislocations in a layer adjacent to the irradiation surface, which is related to a formation of a cellular substructure wherein a part of dislocations is located in cell boundaries and neglected in estimating the scalar dislocation density.

It should be noted that bend extinction contours are absent on micrographs of HEA structures, which indicates that internal stress fields capable of resulting in curvature-torsion of a thin foil are absent in the material. The fact may be indicative of a high plasticity level of the HEA under study that allows a relaxation of internal stress fields by a dislocation slide.

The results obtained in the research suggest a possible increase in a layer hardness at the expense of a substructure with a higher dislocation density in a processed surface and a near-surface layer at a distance up to 45 μm.

The mechanical tests of the HEA in the initial and irradiated states performed by a uniaxial tension of flat proportional samples showed that in the initial state (a state before

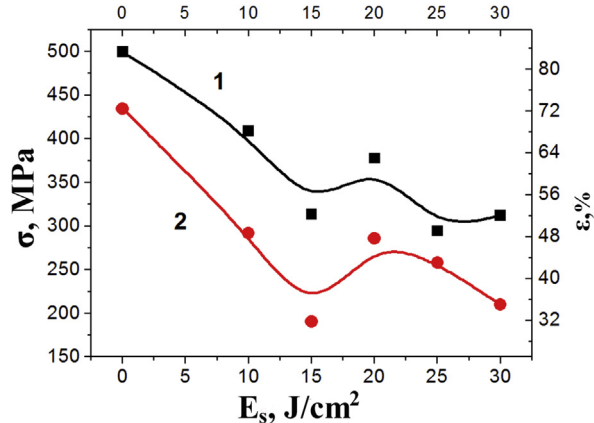


Fig. 6 – The ultimate strength (curve 1) and plasticity (curve 2) as a function of the energy density of an electron beam in the HEA fracture.

irradiation) the alloy has a high level of plasticity (an ultimate plasticity increases 70%) and strength (an ultimate strength reaches 500 MPa) (Fig. 5, curve 1). An irradiation of the alloy with a pulsed electron beam in a regime of a high-speed melting and a subsequent high-velocity crystallization of a surface layer results in a decrease in strength and plasticity of the material (Fig. 5, curve 2). The ultimate values of strength and plasticity of the irradiated HEA vary in a correlated way (Fig. 6).

Concurrently, the HEA irradiation is accompanied with a 1.6-fold decrease in microhardness of the processed layer (from 3.1 GPa before irradiation to 1.85 GPa after irradiation at $E_s = 30 \text{ J}/\text{cm}^2$ (Fig. 7). It is evident that substantial changes in strength and plastic properties of the alloy such as these are due to variations its defective substructure induced by a thermal effect of a pulsed electron beam on the material.

The irradiation of the HEA surface with a pulsed electron beam of a different energy density introduced into the material allowed us to trace an evolution of the alloy defective

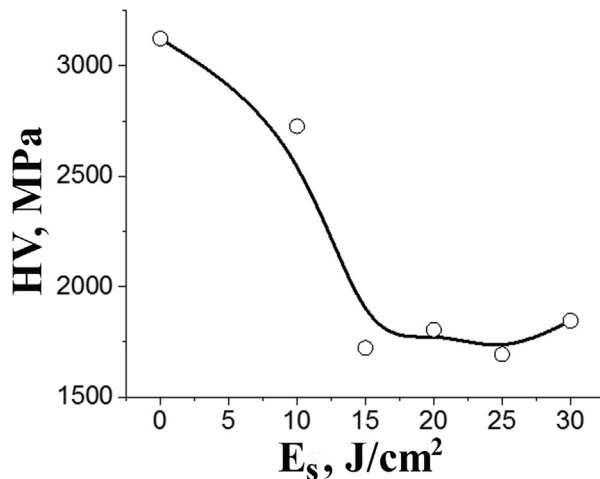


Fig. 7 – Microhardness of the HEA surface layer as a function of the energy density of electron beam.

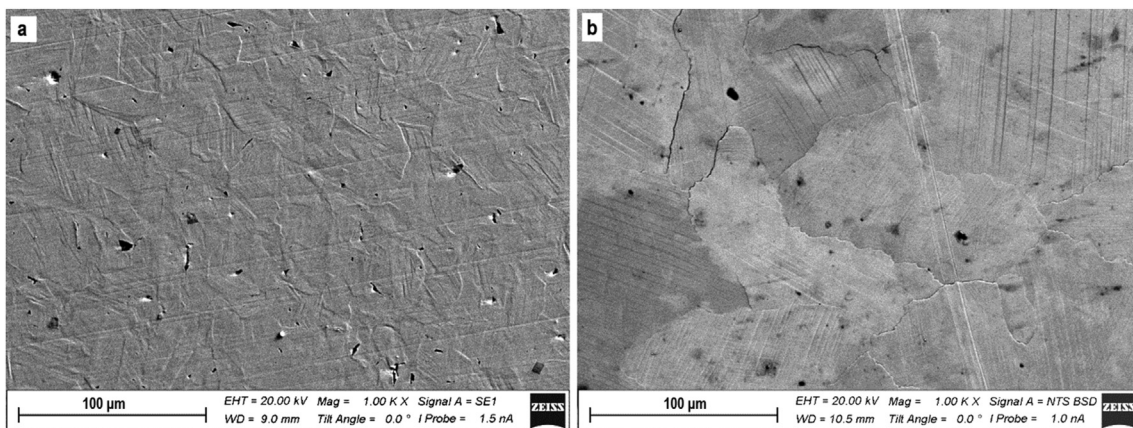


Fig. 8 – A grain structure of the HEA samples before (a) and after (b) irradiation.

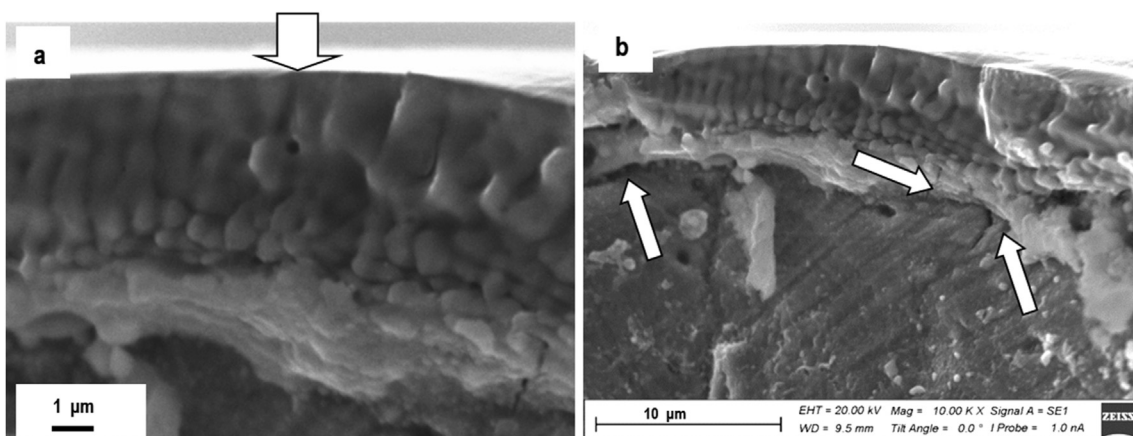


Fig. 9 – A structure of the HEA surface layer crystallization revealed in the analysis of an alloy fracture surface. A – the arrow indicates an irradiation surface; b – microcracks and micropores.

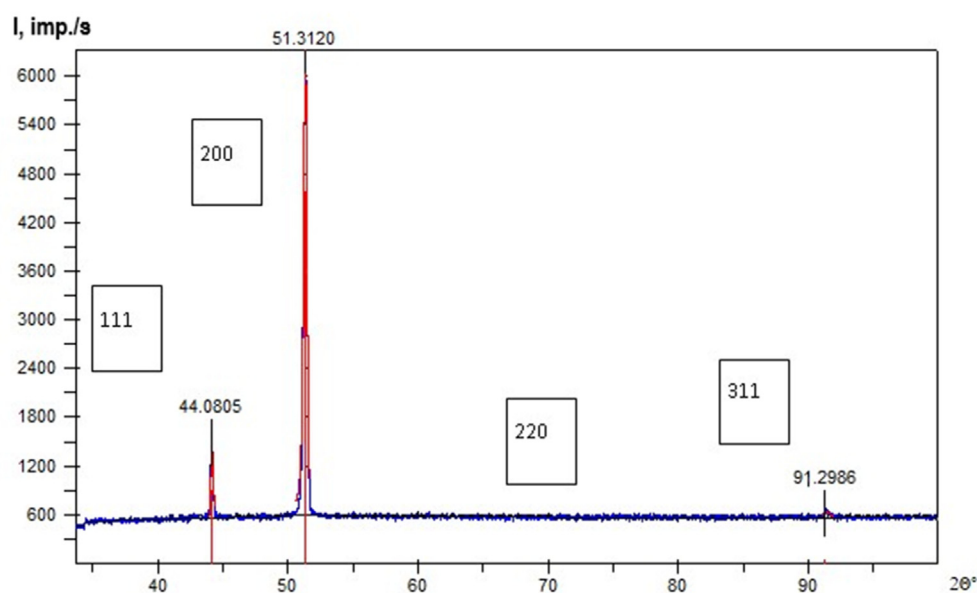


Fig. 10 – A fragment of a X-ray diffraction pattern obtained from the HEA before a pulsed electron beam irradiation (a) and after irradiation at $E_s = 30 \text{ J/cm}^2$.

Table 2 – Results of X-ray diffraction pattern indexing shown in Fig. 10.

| Nº | 2To | 2Tc | 2Tc-2To | d ₀ | d _c | d ₀ -d _c | I | h | k | l |
|----|---------|---------|---------|----------------|----------------|--------------------------------|-------|---|---|---|
| 1 | 44.0810 | 44.0442 | -0.0368 | 2.05270 | 2.05433 | -0.00163 | 19.9 | 1 | 1 | 1 |
| 2 | 51.3126 | 51.3126 | 0.0000 | 1.77910 | 1.77910 | 0.00000 | 100.0 | 2 | 0 | 0 |
| 4 | 91.3019 | 91.7796 | 0.4777 | 1.07720 | 1.07284 | 0.00436 | 1.3 | 3 | 1 | 1 |

Notation: I is the intensity of lines.

2To is the diffraction angle 2θ obtained experimentally.

2Tc is the calculated diffraction angles for K α 1 lines.

d₀ is the experimental interplanar spacing for K α 1 line.

d_c is the calculated interplanar spacing for K α 1 line.

substructure being formed on high-speed heating and cooling. The electron beam irradiation at $E_s = 10 \text{ J/cm}^2$ is accompanied by a process of an alloy primary recrystallization in a surface layer.

Sizes of grains being formed vary in the limits of 1.5–3 μm . The grains locate along grain boundaries of the HEA initial structure. In a bulk of grains not subjected to recrystallization a large number of microtwins is determined. It is suggested that the main reason for twinning of the HEA grains is thermal stresses being formed in the material as a result of a high-speed thermal processing induced by an irradiation.

With a large energy density value of an electron beam ($15\text{--}30 \text{ J/cm}^2$) a process of a collective recrystallization, being accompanied by an increase in grain sizes, develops in the HEA surface layer. An average grain size increases from 35 μm to 120 μm with an increase in the energy density of electron beam from 15 J/cm^2 to 30 J/cm^2 .

The analysis of an irradiation surface structure and a thin surface layer, performed by the methods of scanning and transmission electron microscopy, showed that a high-speed thermal effect, induced by an irradiation, leads to a formation of a cellular crystallization structure in a surface layer. Cells have a low-angle disorientation, as evidenced by an identical contrast on a micrograph (Fig. 8, b). An average size of crystallization cells depends on the energy density of an

electron beam and increases from 310 nm at $E_s = 15 \text{ J/cm}^2$ to 800 nm at $E_s = 30 \text{ J/cm}^2$.

The analysis of a sample fracture surface, being formed in uniaxial tension, showed that thickness of a surface layer, having a cellular structure, amounts to $\approx 5 \mu\text{m}$. Cells have a shape close to equiaxial one and form a columnar structure (Fig. 9). It is noted that the formation of a high-velocity crystallization results in a formation of a micropores' interlayer along a modified layer/main material bulk interface; micro-cracks (Fig. 9, b, micropores and microcracks are indicated by arrows) are determined in a modified layer and an alloy volume adjacent to it.

By the methods of X-ray phase analysis it is established that the HEA, independent of a state under study (initial or irradiated), is a single-phase material and has a face-centered cubic lattice. A characteristic X-ray diffraction pattern of the HEA (initial state) is shown in Fig. 10. The results of X-ray diffraction pattern indexing are presented in Table 2. The studies performed show that the HEA crystal lattice parameter in a state before irradiation is $a = 0.35582 \text{ nm}$.

An irradiation of the alloy, without changing in a crystal lattice type, results in a parameter $a = 0.35574 \text{ nm}$. Concurrently, a redistribution of an intensity of main diffraction peaks is observed, namely, the intensity of peak (111) increases and that of the peak (200) decreases. The latter, obviously, is indicative of a formation of a texture in a surface layer as a result of a high-velocity crystallization. In a quantitative sense the process is presented in Fig. 11.

A phase composition of samples irradiated with a pulsed electron beam was studied by the methods of transmission electron diffraction microscopy through indexing of micro-electron diffraction patterns and applying a technique of dark-field analysis [43–47]. A characteristic electron-microscopic image of the HEA is presented in Fig. 12, a. Analysis of a microelectron diffraction pattern shown in Fig. 12, b revealed a presence of reflections belonging to different phases. Bright reflections form a set of interplanar spacings corresponding to FCC-lattice (a plane of the type $\{110\}$).

The indexing of a microelectron diffraction pattern with regard to elements being present in the alloy allows a suggestion that a phase, having the FCC-lattice and corresponding to the given interplanar spacing, may have the following elemental composition: FeNi or Ni_{2.9}Cr_{0.7}Fe_{0.36}. Along with bright reflections the reflections of a weak intensity are present on a microelectron diffraction pattern (Fig. 12, b, a reflection is indicated by the yellow arrow). The indexing of a microelectron diffraction pattern allows a suggestion that the

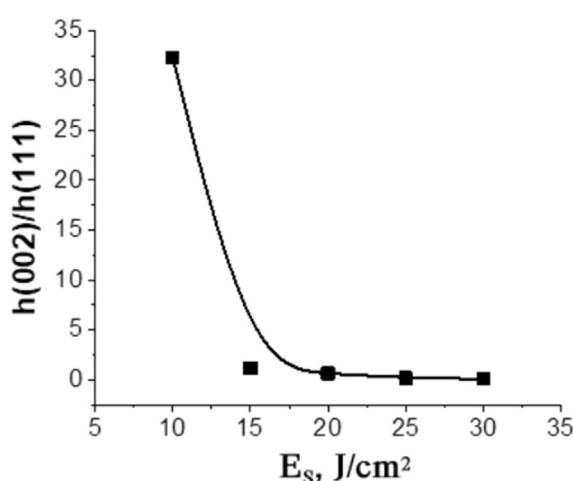


Fig. 11 – A dependence of a relation between intensities of diffraction lines (200) \equiv (002) of the HEA irradiated samples on the energy density of electron beam.

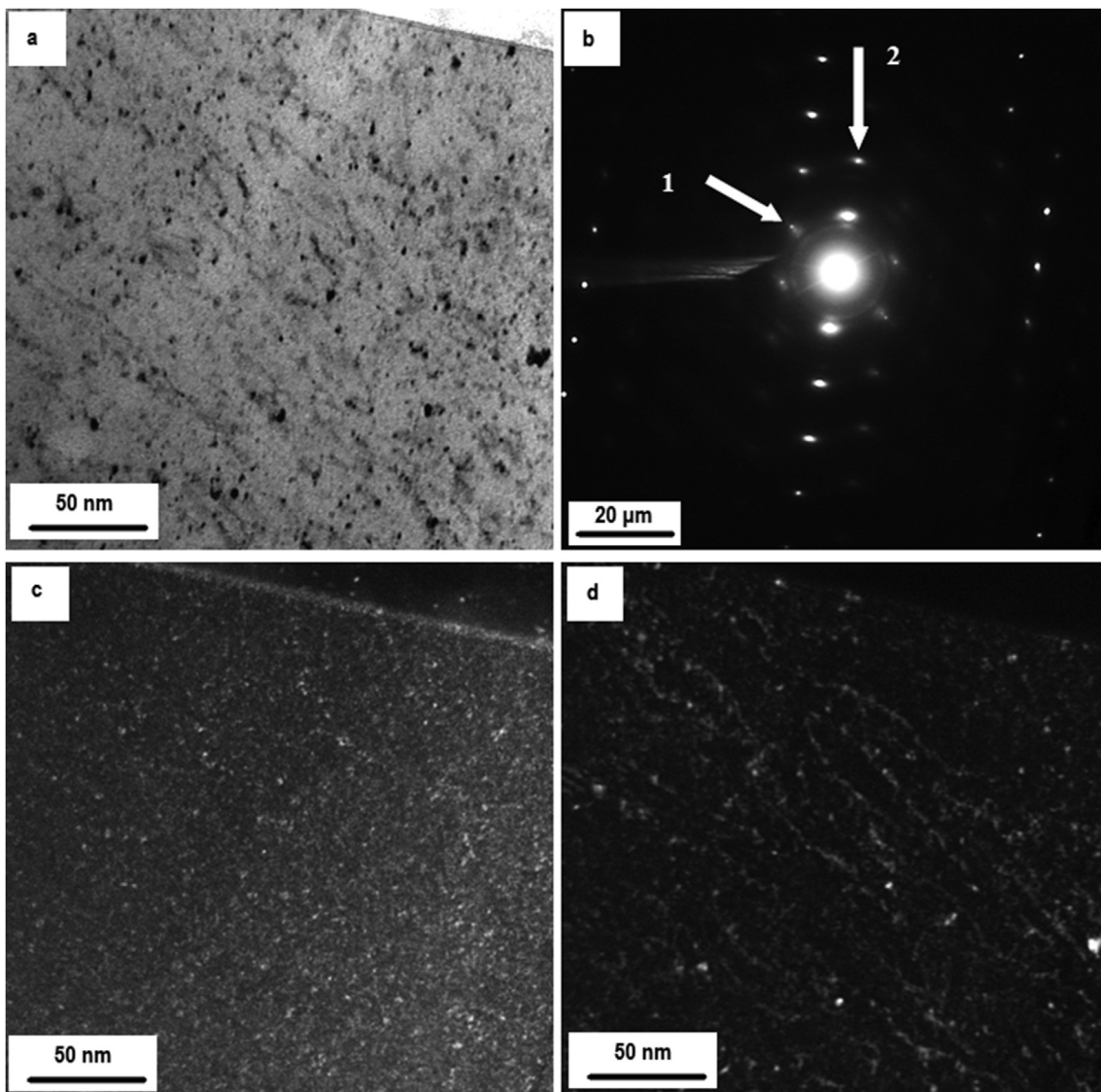


Fig. 12 – A structure of the HEA surface layer irradiated with a pulsed electron beam; a – a bright field; b – a microelectron diffraction pattern; c,d – dark fields obtained in reflections [200] $\text{Ni}_{2.9}\text{Cr}_{0.7}\text{Fe}_{0.36}$ + [200] FeNi + [331] FeCr (c) and [222] $\text{Ni}_{2.9}\text{Cr}_{0.7}\text{Fe}_{0.36}$ + [222] FeNi + [831] FeCr (d). Arrows indicate reflections of dark fields 1 (c), 2 (d).

reflections may belong to the FeCr phase. A dark-field analysis of foil using the reflections indicated in Fig. 12, b by numbers 1 and 2 detected a presence of nanodimensional (1–3 nm) particles in the material. Judging from dark-field images Fig. 12, c, d) the particles have a rounded shape and locate on dislocations. Thus, the irradiation of the HEA with an intense pulsed electron beam results in a decomposition of a solid solution and a precipitation of nanodimensional particles of a second phase.

It was established above by the methods of X-ray structural analysis that the irradiation of the HEA with a pulsed electron beam results in a decrease in the crystal lattice parameter of the alloy from $a = 0.35582$ nm in the initial state to $a = 0.35574$ nm after the irradiation at $E_s = 30 \text{ J/cm}^2$. One of the reasons for it may be a decomposition of a solid solution and an escape of iron and chromium atoms to particles of a second

phase detected by the methods of transmission electron microscopy (Fig. 12). In fact, an average atomic radius of the alloy calculated by additive summation of atomic radii of chemical elements of the alloy with regard to their relative content in the material is equal to $R = 0.127$ nm; an atomic radius of chromium is 0.130 nm, that of iron is 0.126 nm. Therefore, the escape of chromium atoms to second phase particles will contribute to a decrease in the crystal lattice parameter of the alloy.

Actually, the electron microscopic analysis of a samples' fracture surface, along with a ductile pit character of a fracture (Fig. 13, a) revealed a presence of micropores, microlayerings and voids in the material (Fig. 13, b, c). The indicated material defects are very often located on a fracture as extended bands (Fig. 13, d). It is suggested that the location of defects are due to the method of manufacturing of the bulk material.

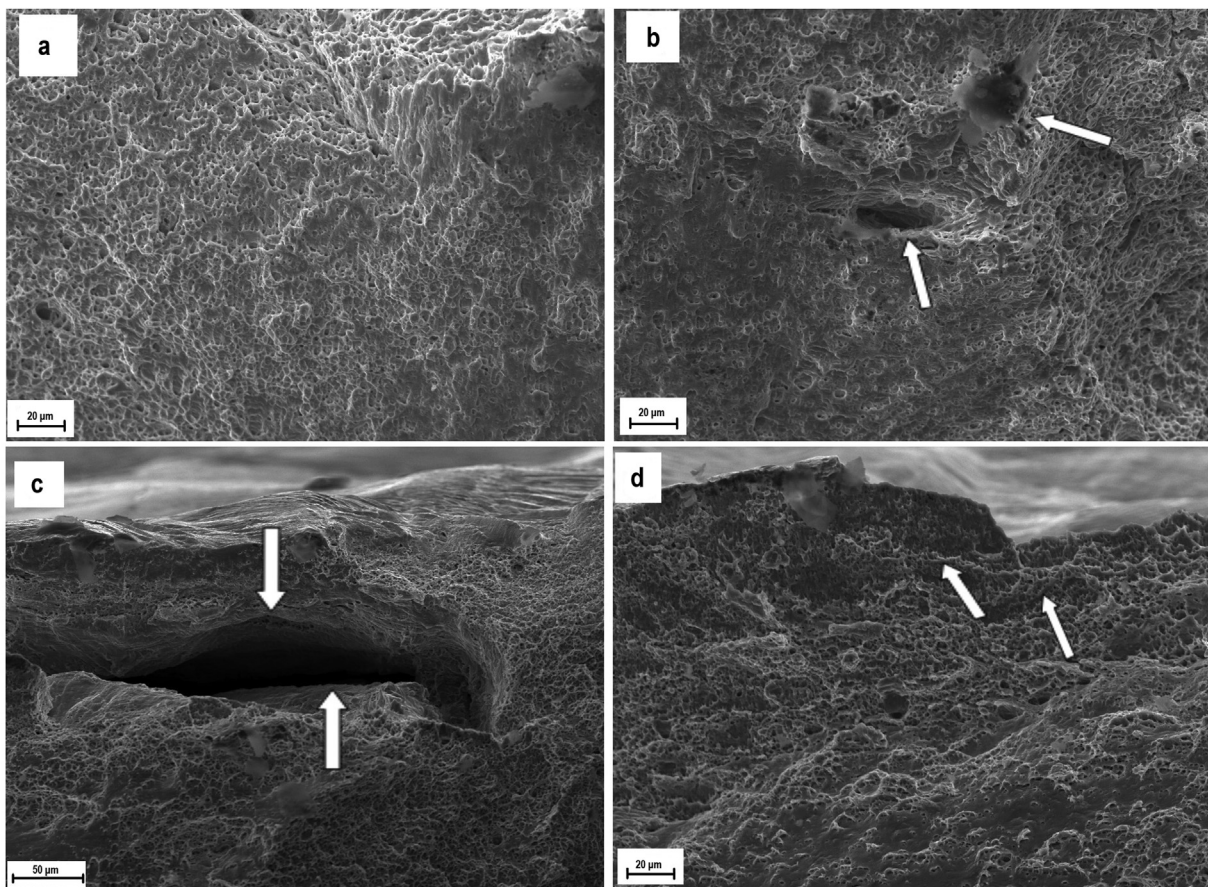


Fig. 13 – The HEA fracture surface in the initial state. a – a ductile pit fracture, b – micropores, c – microlayerings, d – a laminated location of micropores.

The studies of a fracture surface of samples, preliminary irradiated with a pulsed electron beam, detected, along with regions failed according to a ductile mechanism, the material regions, during failure of which, a band (lamellar) structure is formed. Its characteristic image is shown in Fig. 14.

Fracture bands, in most cases, intersect the sample from an upper to a lower edge and locate at an angle of 90° and 45°

to a sample surface. A sample fracture in bands proceeds according to a ductile mechanism too. A diameter of ductile separation pits on fracture bands varies in the limits 0.1–0.2 μm , which is almost an order of magnitude smaller than those of a remaining part of the sample (Fig. 14, a, b).

The studies performed showed that fracture bands of the material did not form in the sample non-irradiated with a

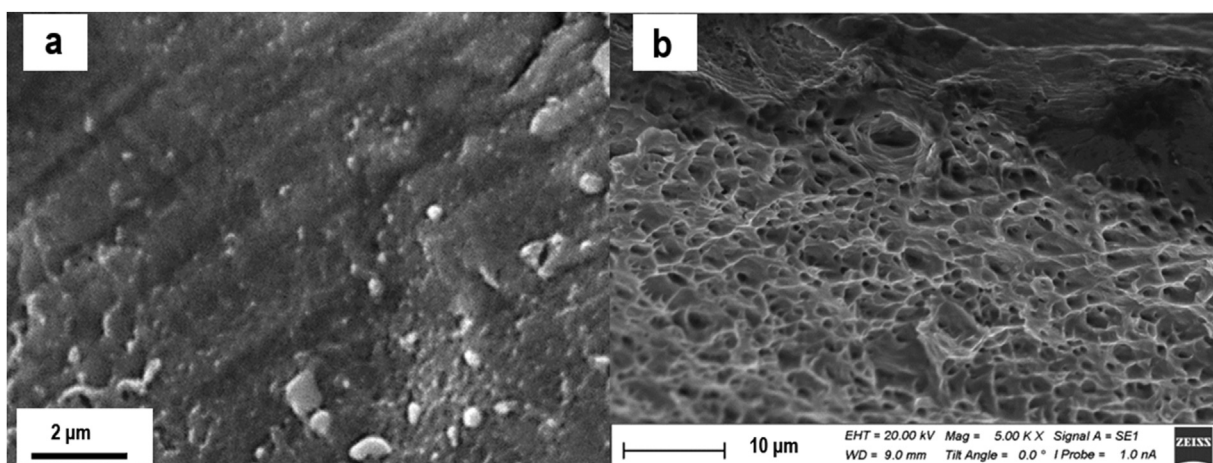


Fig. 14 – A fracture surface of the HEA subjected to a tensile deformation; a) a structure in a fracture band, b) that outside a band. A preliminary irradiation with a pulsed electron beam at $E_s = 30 \text{ J/cm}^2$.

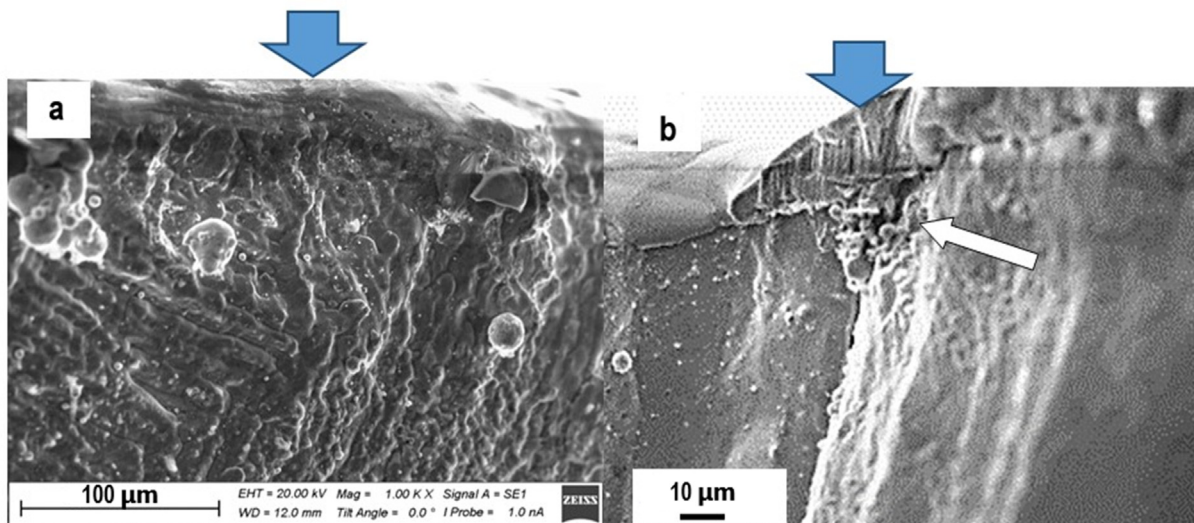


Fig. 15 – A structure of a fracture surface of the sample irradiation with a pulsed electron beam at $E_s = 20 \text{ J/cm}^2$ (a) and $E_s = 25 \text{ J/cm}^2$ (b). Colored arrows indicate an irradiation surface, a light arrow (b) indicates a microcrack.

pulsed electron beam. In the irradiated alloy a size of a material region, whose fracture occurred with a formation of a band structure, increases with a growth in the energy density of electron beam, namely, at $E_s = 10 \text{ J/cm}^2$ regions with a band structure occupy $\approx 25\%$ of a fracture area, at $E_s = 30 \text{ J/cm}^2 \approx 65\%$. It is suggested that a band structure formation at the HEA fracture is one of reasons for decreasing the ultimate strength and plasticity of the material in an irradiated state.

The study of a fracture surface of the HEA samples allowed us to estimate a thickness of a molten layer and to consider a state of a boundary (melt/solid) layer being formed in a metal high-velocity crystallization being realized as a result of the irradiation with a pulsed electron beam. The studies carried out showed that the thickness of a molten layer varies in the limits from $0.8 \mu\text{m}$ to $5 \mu\text{m}$ and increases with a growth in the energy density of electron beam (Fig. 15).

Sizes of crystallites of the layer practically coincide with sizes of crystallization cells indicated above. The HEA volume modified by electron beam has a two-layer structure. Micro-pores locate at a surface-subsurface layer interface as well as a subsurface layer and main bulk of the alloy. A subsurface layer and a sample bulk adjacent to it contain microcracks located mostly at right angle to the sample surface (Fig. 15, b). In a surface layer such cracks are not detected. It is suggested that defects revealed in surface and subsurface layers form as a result of elastic stresses originating in high-speed quenching of samples after completing a thermal effect of electron beam. The defects may also be a reason for decreasing in the ultimate strength and plasticity of the material in the irradiated state.

4. Conclusion

By means of the wire-arc additive manufacturing technology the samples of the CoCrFeMnNi high-entropy alloy of a non-equatomic composition has been fabricated. By the methods of modern physical materials science the studies of structure,

phase composition, defective substructure, properties and fracture surface of the HEA subjected to the electron-beam processing (with the parameters: the energy density of electron beam $10\text{--}30 \text{ J/cm}^2$, duration $50 \mu\text{s}$, pulse repetition rate 0.3 s^{-1} , pulse number 3) were carried out.

It is stated that the alloy before irradiation is a single-phase material having a face-centered crystal lattice. The irradiation of the alloy with a pulsed electron beam results in no change in its elemental composition, however, transforms substantially its defective substructure. Firstly, it results in a considerable (by 6 times, from $20 \mu\text{m}$ to $120 \mu\text{m}$) increase in an average grain size. Secondly, it leads to a formation of a high-velocity cellular crystallization with cell sizes of $400\text{--}550 \text{ nm}$ in a surface layer $\approx 5 \mu\text{m}$ thick. Thirdly, it acts to a formation of a high-velocity crystallization texture of a molten surface layer. Fourthly, it produces a decomposition of a solid solution with a precipitation of nanodimensional particles of FeCr composition. It is shown that the irradiation with a pulsed electron beam results in a formation of a gradient dislocation structure. In a surface layer a nondisoriented cellular dislocation structure is formed. Chaotically distributed dislocations are observed in its volume of cells. At a depth of $25 \mu\text{m}$ a nondisoriented cellular-netlike dislocation substructure with the greatest dislocation density of $\sim 5.5 \cdot 10^{10} \text{ cm}^{-2}$ is formed. At a depth of $45 \mu\text{m}$ a structure, formed by dislocations distributed chaotically, is present along with a cellular-netlike dislocation substructure. In total, it resulted to a decrease in plasticity by more than 2 times, strength by 1.3 times, microhardness by 1.6 times of the irradiated alloy relative to a nonirradiated state.

Declaration of Competing Interest

The authors declare that they have no known competing financial interests or personal relationships that could have appeared to influence the work reported in this paper.

Acknowledgements

The research was supported by Russian Research Foundation grant (project № 20-19-00452).

REFERENCES

- [1] George EP, Curtin WA, Tasan CC. High entropy alloys: a focused review of mechanical properties and deformation mechanisms. *Acta Mater* 2020;188:435–74.
- [2] Shivam V, Basu J, Pandey VK, Shadangi Y, Mukhopadhyay NK. Alloying behaviour, thermal stability and phase evolution in quinary AlCoCrFeNi high entropy alloy. *Adv Powder Technol* 2018;29:2221–30.
- [3] Ganesh UL, Raghavendra H. Review on the transition from conventional to multi-component-based nano-high-entropy alloys—NHEAs. *J Therm Anal Calorim* 2020;139:207–16.
- [4] Alshataif YA, Sivasankaran S, Al-Mufadi FA, Alaboodi AS, Ammar HR. Manufacturing methods, microstructural and mechanical properties evolutions of high-entropy alloys: a review. *Met Mater Int* 2019;26:1099–133.
- [5] Cheng KC, Chen JH, Stadier S, Chen SH. Properties of atomized AlCoCrFeNi high-entropy alloy powders and their phase-adjustable coatings prepared via plasma spray process. *Appl Surf Sci* 2019;478:478–86.
- [6] Joseph J, Hodgson P, Jarvis T, Wu X, Stanford N, Fabijanic DM. Effect of hot isostatic pressing on the microstructure and mechanical properties of additive manufactured $\text{Al}_x\text{CoCrFeNi}$ high entropy alloys. *Mater Sci Eng* 2018;733:59–70.
- [7] Jian R, Wang L, Zhou S, Zhu Y, Liang YJ, Wang B, et al. Achieving fine-grain tungsten heavy alloys by selecting a high entropy alloy matrix with low W grain growth rate. *Mater Lett* 2020;278:128405.
- [8] Hou L, Hui J, Yao Y, Chen J, Liu J. Effects of boron content on microstructure and mechanical properties of AlFeCoNiBx high entropy alloy prepared by vacuum arc melting. *Vacuum* 2019;164:212–8.
- [9] Wu H, Huang S, Zhao C, Zhu H, Xie Z, Tu C, et al. Microstructures and mechanical properties of in-situ FeCrNiCu high entropy alloy matrix composites reinforced with NbC particles. *Intermetallics* 2020;127:106983.
- [10] Xu Y, Li C, Huang Z, Chen Y, Zhu L, Zhang Y. Microstructure evolution and mechanical properties of $\text{FeCoCrNiCuTi}_{0.8}$ high-entropy alloy prepared by directional solidification. *Entropy* 2020;22:1–12.
- [11] Liu Y, Zhang Y, Zhang H, Wang N, Chen X, Zhang H, et al. Microstructure and mechanical properties of refractory $\text{HfMo}_{0.5}\text{NbTiV}_{0.5}\text{Si}_x$ high-entropy composites. *J Alloys Compd* 2017;694:869–76.
- [12] Zhang Y, Han T, Xiao M, Shen Y. Effect of Nb content on microstructure and properties of laser cladding $\text{FeNiCoCrTi}_{0.5}\text{Nb}_x$ high-entropy alloy coating. *Optic* 2019;198:163316.
- [13] Tabachnikova ED, Shapovalov YuA, Smirnov SN, Gorban VF, Krapivka NA, Firstov SA. Low-temperature mechanical properties and thermally activated plasticity parameters of the $\text{CrMnFeCoNi}_2\text{Cu}$ high entropy alloy. *Low Temp Phys* 2020;46(9):1131–41.
- [14] Nadutov VM, Volosevich PYu, Proshak AV, Panarin VE, Svalivny NE. Structure of ion-plasma coatings from the AlFeNiCoCuCr high-entropy alloy. *Metallophysics Adv Technol* 2017;39(11):1525–45.
- [15] Rempel AA, Gel'chinskii BR. High-entropy alloys: preparation, properties and practical application. *Izvestiya. Ferrous Metallurgy*. 2020;63(3–4):248–53.
- [16] Rogachev AS. Structure, stability and properties of high-entropy alloys. *Phys Metals Mater Sci* 2020;121(8):807–41.
- [17] Bashev VF, Kushnerov Ol. Structure and properties of cast and splat-quenched high-entropy Al–Cu–Fe–Ni–Si alloys. *Phys Met Metallogr* 2017;118(1):39–47.
- [18] Shaysultanov D.G., Stepanov N.D., Salishchev G.A., Tikhonovsky M.A. Effect of heat treatment on the structure and hardness of high-entropy alloys CoCrFeNiMnV_x ($x = 0.25, 0.5, 0.75, 1$). *Phys Met Metallogr*. 201;118(6):579–590.
- [19] Miracle DB, Senkov ON. A critical review of high entropy alloys and related concepts. *Acta Mater* 2017;122:448–511.
- [20] Zhang W, Liaw PK, Zhang Y. Science and technology in high-entropy alloys. *Sci China Earth* 2018;61:2–22.
- [21] Osintsev KA, Gromov VE, Konovalov SV, Ivanov YuF, Panchenko IA. High-entropy alloys: structure, mechanical properties, deformation mechanisms and application. *Izvestiya. Ferrous Metallurgy*. 2021;64(4):249–58.
- [22] Gromov VE, Konovalov SV, Ivanov YuF, Osintsev KA. Structure and properties of high-entropy alloys. Springer; 2021. Advanced structured materials.
- [23] Ivanov YuF, Gromov VE, Konovalov SV, Shliarova YuA. Evolution of structure of AlCoCrFeNi high-entropy alloy on irradiation by pulsed electron beam. *J Appl Phys* 2021;91(12):1971–4.
- [24] Zhang T, Xin L, Wu F, Xiang Chen J, Jiang S, Huang Y, et al. Microstructure and mechanical of $\text{Fe}_x\text{CoCrNiMn}$ high-entropy alloys. *J Mater Sci Technol* 2019;35(10):2331–5.
- [25] Gludovatz B, Hohenwarter A, Catoor D, Chang EH, George EP, Ritchie RO. Fracture-resistant high-entropy alloy for cryogenic applications. *Sci* 2014;345(6201):1153–8.
- [26] Yamanaka S, Ikeda R, Miura S. The effect of titanium and silicon addition on phase equilibrium and mechanical properties of CoCrFeMnNi -based high entropy alloy. *J Mater Res* 2021;36(10):2056–70.
- [27] Xian X, Lin L, Zhong Z, Zhang C, Chen C, Song K, et al. Precipitation and its strengthening of Cu-rich phase in CrMnFeCoNiCu_x high-entropy alloys. *Mater Sci Eng* 2018;713:134–40.
- [28] Lu Y, Mazilkin A, Boll T, Stepanov N, Zherebtsov S, Salishchev G, et al. Influence of carbon on the mechanical behavior and microstructure evolution of CoCrFeMnNi processed by high pressure torsion. *Materialia* 2021;16:101059.
- [29] Listyawan TA, Lee H, Park N, Lee U. Microstructure and mechanical properties of CoCrFeMnNi high entropy alloy with ultrasonic nanocrystal modification process. *J Mater Sci Technol* 2020;57:123–30.
- [30] Meng F, Baker I. Nitriding of a high entropy FeNiMnAlCr alloy. *J Alloys Compd* 2015;645:376–81.
- [31] Panin SV, Ilasov IV, Sergeev VP, Maruschak PO, Sunger R, Ovechkin BB. Fatigue life improvement of $12\text{Cr}1\text{MoV}$ steel by irradiation with Zr^+ ion beam. *Phys Mesomech* 2015;18:261–72.
- [32] Lindner T, Lobel M, Sattler B, Lampke T. Surface hardening of FCC phase high-entropy alloy system by powder-pack boriding. *Surf Coating Technol* 2019;371:389–94.
- [33] Proskyrovsky Dl, Rotshtein VP, Ozur GE, Ivanov YF, Markov AB. Physical foundations for surface treatment of materials with low energy, high current electron beams. *Surf Coating Technol* 2000;125(1–3):49–56.
- [34] Valkov S, Ormanova M, Petrov P. Electron-beam surface treatment of metals and alloys: techniques and trends. *Metals* 2020;10(9):1–20.
- [35] Konovalov S, Ivanov Y, Gromov V, Panchenko I. Fatigue-induced evolution of ALSI 310S steel microstructure after electron beam treatment. *Materials* 2020;13(20):4567.
- [36] Zhang C, Lv P, Xia H, Yang Z, Konovalov S, Chen X, et al. The microstructure and properties of nanostructured CrAl alloying layer fabricated high-current pulsed electron beam. *Vacuum* 2019;167:263–70.

- [37] Konovalov SV, Komissarova IA, Kosiniv DA, Ivanov YF, Gromov VE. Structure of titanium alloy, modified by electron beams and destroyed during fatigue. *Letters on Materials* 2017;7(3):266–71.
- [38] Lyu P, Peng T, Miao Y, Liu Z, Gao Q, Zhang C, et al. Microstructure and properties of CoCrFeNiMo0.2 high-entropy alloy enhanced by high-current pulsed electron beam. *Surf Coating Technol* 2021;410:126911.
- [39] Cai J, Yao Y, Gao C, Lyu P, Meng X, Guan Q, et al. Comparison of microstructure and oxidation behavior of NiCoCrAlYSi laser cladding coating before and after high-current pulsed electron beam modification. *J Alloys Compd* 2021;881:160651.
- [40] Osintsev K, Gromov V, Ivanov Y, Konovalov S, Panchenko I, Vorobyev S. Evolution of structure in alcocrfeni high-entropy alloy irradiated by a pulsed electron beam. *Metals* 2021;11:1228.
- [41] State Standard 1497-84. Metals. Methods of tensile test. M.: Standartinform; 2005.
- [42] Koval NN, Ivanov YuF. Nanostructurization of surface of metal-ceramic and ceramic materials at pulsed electron-beam processing. *Russ Phys J* 2008;51(5):505–16.
- [43] Utevsky LM. Diffraction electron microscopy in physical metallurgy. M.: Metallurgia; 1973.
- [44] Tomas G, Goringe MJ. Transmission electron microscopy of materials. M. Nauka; 1983.
- [45] Egerton FR. Physical principles of electron microscopy. Basel: Springer International Publishing; 2016.
- [46] Kumar CSSR. Transmission electron microscopy. Characterization of nanomaterials. New York: Springer; 2014.
- [47] Carter CB, Williams DB. Transmission electron microscopy. Berlin: Springer International Publishing; 2016.